




Cascade model for continuous prediction of silicon content of molten iron with coupled state variable nodes

Yang Han^{1,2} · Ze-qian Cui^{1,2} · Li-jing Wang^{1,2} · Jie Li^{1,2}  · Ai-min Yang¹ · Yu-zhu Zhang²

Received: 16 July 2022 / Revised: 21 December 2022 / Accepted: 26 December 2022 / Published online: 2 March 2023
© China Iron and Steel Research Institute Group Co., Ltd. 2023

Abstract

With the goal of achieving advanced and multi-step prediction of silicon content of molten iron in the blast furnace ironmaking process, a path adaptive optimization seeking strategy coupled with simulated annealing algorithm and genetic algorithm was proposed from the perspective of innovative intelligent algorithm application. It was further coupled with wavelet neural network algorithm to deeply explore the nonlinear and strong coupling relationship between the information of big data samples and construct a cascade model for continuous prediction of silicon content of molten iron with the intelligent research results of state variables such as permeability index as the node and silicon content forecast as the output. In the model construction process, the 3σ criterion was used for non-anomaly estimation of abnormal data to build a time-aligned sample set for multi-step forecasting of iron content, the normalization method was used to eliminate the influence of dimensionality of sample information, and the spearman correlation analysis algorithm was used to eliminate the time delay between state variables, control variables, and silicon content of molten iron in the blast furnace smelting process. The results show that permeability and theoretical combustion temperature as the key state variable nodes have real-time correlation with the silicon content of molten iron, and there are accurate forecasting results on the optimal path with the endpoint of molten iron silicon content prediction. The path finding based on the improved genetic algorithm of simulated annealing has good effect on the downscaling and depth characterization of sample data and improves the data ecology for the application of wavelet neural network algorithm. The accuracy of the real-time continuous forecasting model for the silicon content of molten iron reaches 95.24%; the hit rate of continuous forecasting one step ahead reaches 91.16%, and the hit rate of continuous forecasting five steps ahead is 87.41%. This model, which can realize the nodal dynamics of state variables, has better promotion value.

Keywords Silicon content · Molten iron · Optimal path · State variable node · Wavelet neural network · Step-by-step prediction

1 Introduction

The silicon content of the molten iron, which is the final product of the blast furnace, not only reflects the quality of the molten iron, but also characterizes the thermal state of

the blast furnace. Therefore, the accurate prediction of the silicon content of the molten iron is very important for the operation of the blast furnace [1]. However, the blast furnace smelting system involves a complex set of heat transfer and chemical reactions, with internal momentum, heat, and mass transfer coupling. During smelting, blast furnace gases rise and fall; the internal phase transformation of gas–solid–liquid phase-oriented fluidity of the blast furnace constantly evolves in an extremely complex process with nonlinear, strong coupling and large time delay characteristics. Relying solely on mechanistic analysis and mathematical models of the smelting process makes continuous and accurate prediction of the molten iron silicon content difficult [2–4]. Therefore, effectively using

✉ Jie Li
lijie-2573017@163.com

¹ Hebei Engineering Research Center for the Intelligentization of Iron Ore Optimization and Ironmaking Raw Materials Preparation Processes, North China University of Science and Technology, Tangshan 063210, Hebei, China

² College of Metallurgy and Energy, North China University of Science and Technology, Tangshan 063210, Hebei, China

technological innovation-driven ironmaking blast furnaces and achieve continuous prediction of the molten iron silicon content is an increasingly important requirement for intelligent manufacturing in the steel industry.

Large-scale data have been linked, integrated, and fused, providing renewed impetus and opportunities for collaborative development in various industries. Given the rapid technological changes and enormous data availability, exploring fusion data techniques to support complex decision-making and provide deep insight through data mining has become key support and core competitive advantage [5]. Global science and technology development and national strategic needs have focused increasingly on big-data management. Moreover, the metallurgical industry in China is facing problems under the “new normal” of the Chinese economy. Consequently, the harsh market conditions have forced the steel industry to vigorously develop intelligent metallurgical manufacturing technologies with data at their core.

China’s steel industry generates multi-source multi-modal data, accurately portraying the production process. Most data are discarded as they are considered “invalid” [6], but these data can be rich in information, making it important to combine different modal data sources to conduct deep data mining and fusion modeling [7]. Existing blast furnace big-data research uses artificial intelligence algorithms to model complex processes, ignoring complex process mechanisms and using data-driven technology to determine quantitative relationships between variables. Based on the general rules of blast furnace smelting process mechanism and transient process, a model was designed to predict the silicon content of iron 10 h ahead of time based on the specific blast furnace boundary conditions, taking into account the iron ore raw material and coke quality. The root-mean-square deviation between the obtained predicted iron silicon content and the actual measured value is 0.09% [8]. In Ref. [9], a new multi-input multi-output (MIMO) Takagi–Sugeno (T-S) fuzzy model was proposed using an output transfer matrix. By explicitly modeling inter-indicator correlations through low-rank learning of the correlation matrix, the great challenge of jointly determining the MIMO T-S model and the fuzzy rules for inter-indicator correlations is overcome. And a better prediction result for the silicon content of molten iron was achieved even with a sample missing rate of 90%. In order to overcome the difficulties caused by the nonlinear time-varying dynamics of the process and to enable random vector functional-link network (RVFLN) to learn online and avoid data saturation, by sequential learning with forgetting factors and applying the Cauchy distribution function to properly evaluate the weights of different data, good modeling accuracy was achieved for outlier contamination rates up to 50% and for anomaly magnitudes

up to 5 times the difference between the maximum and minimum values of each output [10]. The T-S fuzzy modeling method based on Bayesian block structure sparsity for continuous prediction of silicon content of molten iron. By this method, the main important fuzzy rules and the corresponding pivotal result parameters can be automatically selected to obtain compact fuzzy models with good generalization performance [11]. The effect of parameter variations on the silicon content was determined by differential processing and correlation analysis [12]. The Elman silicon content prediction model and logistic furnace temperature fluctuation prediction model were developed [13]. The adaptive density peak clustering of the Bonferroni index and a multi-source path finding algorithm were combined to construct a method to predict the silicon content of molten iron in blast furnace based on optimal work migration [14].

Based on the above analysis, it is important to understand the meaning of data-driven technology: “deep mining of universal laws among sample information in known, incomplete or imprecise measurement results of big data (samples)” [15]. The data information collected during the blast furnace smelting process can be divided into “control variables” and “state variables” according to their functions; the data information collected during the blast furnace smelting process can also be divided into “sample input” and “sample output” according to the structure of the data-driven model sample set. For the “sample input” and the “sample output”, the sample input index data are ahead of the sample output and are easier to obtain than the output index. Obviously, the sample input is the state variable, which is ahead of the sample output (silicon content of molten iron) for continuous prediction and needs to consider the control variables such as coal injection volume and state variables such as permeability index, but the state variables will change with the control variables. In addition, the volume of the blast furnace is huge, and the gas–solid–liquid phase fluidity exists inside the blast furnace. The physical and chemical reactions in different parts of the blast furnace are significantly different. This difference makes the blast furnace have obvious thermal hysteresis and chemical hysteresis to the step of control parameters and the fluctuation of raw and fuel properties and compositions. There are intermittent and continuous, real-time and delay relationships in the process of setting and adjusting process parameters. To this end, based on the sample information to complete the spatiotemporal alignment between sample information and form data-driven samples with certain correspondence, a path adaptive model using simulated annealing algorithm to optimize the genetic algorithm is proposed, and this improved model is coupled with wavelet neural network algorithm to deeply explore the nonlinear and strong coupling relationship

between large data sample information in the blast furnace smelting process and realize a model with permeability index. The model is a continuous forecasting model with the prediction of state variables such as permeability index as the node and the prediction of silicon content of molten iron as the endpoint.

2 Model for controlling silicon content of molten iron in blast furnace

The mathematical model mechanisms of the blast furnace smelting process are primarily based on hydrodynamic and metallurgical reaction kinetics.

- (1) The blast furnace smelting process can be examined from a fluid dynamics perspective. The “downward fluid” movement comprises the movement of raw fuel loaded at the furnace top under high-temperature physicochemical conditions. The “upward fluid” movement includes movement of the blast air, coal injection entering via the air outlet, and the resulting fluid movement in the plant from the chemical reactions. The applicable universal laws of fluid science are the mass conservation equation, equation of fluid motion, and equation of state of matter [16]. Considering only the fluid in the blast furnace axial z -direction moving at a material speed (v_{LS}) and ignoring the radial (r) and annular (θ) effects on the movement speed, the simplified blast furnace fluid dynamics mathematical model can be expressed as follows:

$$\frac{\partial \rho}{\partial t} + \frac{\partial \rho v_{LS}}{\partial z} = k\rho$$

$$\frac{dv_{LS}}{dt} = G - \frac{1}{\rho} \frac{Q_{fq}}{F_f} \tag{1}$$

where Q_{fq} is the air volume; ρ is the fluid density; k is the scale factor; F_f is the permeability index, defined as the ratio of air volume to differential pressure P , that is, $F_f = Q_{fq}/\text{grad } P$; t is the time; and G is gravity.

- (2) The chemical reaction in blast furnace smelting process is the chemical reaction in fluid motion. From the perspective of mathematical modeling, more than 100 chemical reactions in blast furnace are abstracted into generalized chemical reaction equations ($A + B = F + G + U_m \cap (T_s \text{ and } p \text{ and } w)$) i [17], where A and B are reactants, F and G are products, and U_m denotes the thermal effect of the reaction process. The model constraints are the

starting temperature T_s , pressure p , and concentration of reactants w required for the i th chemical reaction to proceed. Only chemical reactions that satisfy these constraints occur. Analyzed from the viewpoint of mathematical planning models, it constitutes a special mathematical planning problem—a microscopic, large scale, dynamic linear programming problem.

The intricate correlation of the two kinetic models causes extremely complex variations in the silicon content of molten iron. Figure 1 shows the migration trends of silicon content of molten iron in the longitudinal direction of the blast furnace, starting from the middle of the furnace to the window area. The silicon content increases with increasing carbon in the molten iron, reaching a maximum in the window area, and is higher than that in the final iron. Only the silicon content in the metal directly above the window is close to the outgoing iron value as silicon continues to enter the pig iron below the window [18]. Silicon is absent in the metal in the soft melt before the drip zone, and it is only in the high-temperature zone after the drip zone that silicon gradually enters the pig iron.

A prerequisite for predicting the silicon content of molten iron is to clarify the silicon source, which determines the interval for estimating the silicon content of molten iron. Based on the material balance, SiO_2 from the coke ash can supply the silicon needed for low-silicon iron in the form of SiO . However, as it is available in limited quantities (Table 1), silicon should also be obtained from the slag when smelting other iron types. Consequently, the thermodynamically permissible silicon content in blast

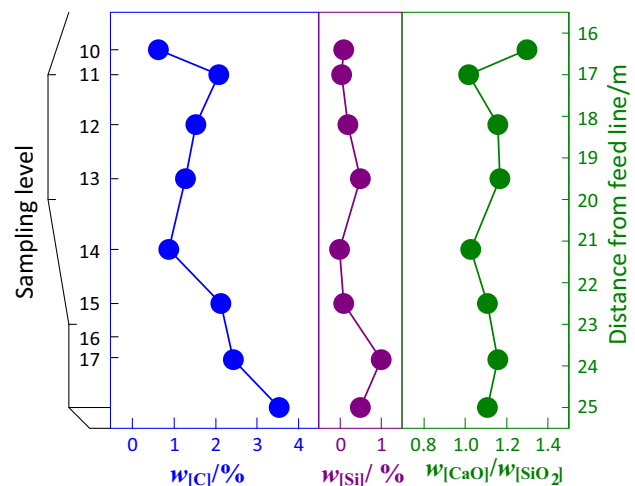


Fig. 1 Metal iron and slag composition migration trends along longitudinal direction of blast furnace

Table 1 Maximum amount of silicon supplied by different coke ratios (kg/t)

Coke ratio	400	500	600	700	800	900	1000
Maximum Si amount	11.2	14.0	16.8	19.6	22.4	26.2	28.0

furnace pig iron is much greater than the actual quantity of silicon supplied via coke ash. Moreover, the silicon reduction is governed by kinetic conditions such as the molten iron temperature and SiO₂ activity in the slag.

A reasonable approach is to express the relationship between the thermal regime and the silicon in the pig iron in terms of the heat balance established by the volume of gas, the amount of material, and the respective temperature levels in the high-temperature zone below the drip zone. The residence time of the iron droplets in the reaction zones, that is, the gas–liquid contact time (*t*) in relation to the smelting cycle (*τ*) and drip zone height (*h*), is overlooked. Under countercurrent conditions, an increase or decrease in the iron solution residence time should be expressed as an increase or decrease in the residence time of the gas in this zone. Because there is no change in the amount of heat consumed per unit time and that supplied by the gas, the residual time (*τh/H*, where *H* is the height of blast furnace body) is eliminated when calculating the silicon content in pig iron.

To determine the estimated silicon content in the molten iron based on material balance, the blast furnace supervisor can evaluate the relevant fluctuation patterns by adjusting the key controlling parameters, such as the material speed, permeability index, air volume, and coal injection amount (*Q_{pm}*). The air volume and the coal injection are related to fluid dynamics, while the material speed and the permeability index are related to chemical reaction kinetics and state variables of fluid dynamics. The partial differential equation for variations in the silicon content of molten steel can be expressed as follows:

$$\frac{dw_{[Si]}}{dt} = L(t) \frac{\partial v_{LS}}{\partial t} + F(t) \frac{\partial F_f}{\partial t} + Q(t) \frac{\partial Q_{fq}}{\partial t} + M(t) \frac{\partial Q_{pm}}{\partial t} \tag{2}$$

where *L(t)*, *F(t)*, *Q(t)*, and *M(t)* represent the influence coefficients of the differential terms material speed, permeability index, air volume, and coal injection amount, respectively, and are nonlinear functions that vary with furnace temperature and index conditions.

Through the above analysis, the estimation interval and the variation mechanism of the silicon content of molten iron can be determined. Consequently, a big data mining study of the blast furnace smelting process was conducted to achieve the multi-step prediction of the silicon content of molten iron continuously and accurately by incorporating data-driven technology.

3 Time registration between big data and sample information in blast furnace smelting process

3.1 Determining data index category of blast furnace smelting process based on control theory

The blast furnace is an inertial system from a control perspective. When many control parameters (actions) change, it causes a lag of state parameters. The possible lags and the corresponding response law should be digitally expressed to realize intelligent prediction and control of the blast furnace smelting process. Moreover, a certain transition is required when the blast furnace changes from one stable state to another. The first-order response, as expressed in Eq. (3), can schematically characterize the response process of the silicon content of molten iron, as shown in Fig. 2.

$$y(t + t_D) = Kx - T \frac{dy(t + t_D)}{dt} + y_0 \tag{3}$$

where *x* denotes a step, that is, a control parameter; *t_D* is the time delay; *T* is the time constant; *y* is the final effect; *K* is the gain; *y₀* denotes the response with time *t* = 0; and *y(t + t_D)* denotes the response with time *t*. After a step is sent, a response can only occur after a time delay, reaching a stable state after a period of 4 *T* or 5 *T*. Hence, the actual period from changing a control parameter to obtaining the desired response is *t_D* + 4 *T* or *t_D* + 5 *T*.

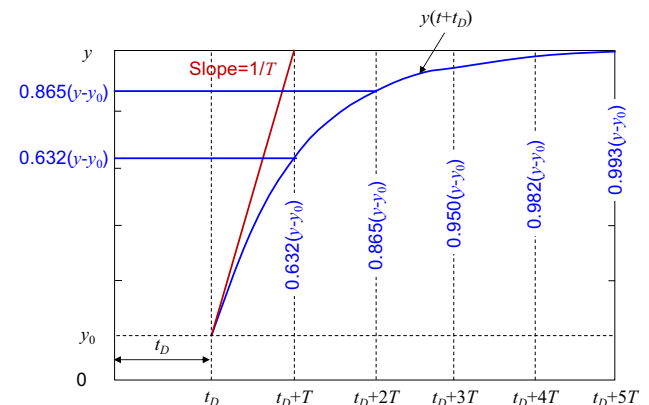


Fig. 2 Schematic of first-order response process of silicon content in molten iron

Several parameters (including interference) often play a key role in strengthening or weakening the changes in the silicon content of molten iron. Often, other parameters can change before the completion of specific behavior, which can positively or negatively impact the previous transition behavior, resulting in a complex transition behavior. Consequently, the big data from the blast furnace smelting process should be further classified from a control system perspective.

- (1) Control variables are the variables controlled when the blast furnace length adjusts the operational state of the blast furnace. It comprises the relevant variables of the upper distribution and lower blast systems. Typical indicators include blast volume, blast temperature, blast humidity, coal injection volume, oxygen enrichment rate, pulverized coal composition, hot air pressure, and air pressure.
- (2) State variables are the primary performance indicators that measure the operational state of the blast furnace. These variables are concentrated in the blast furnace body.

3.2 Big data sample set of blast furnace smelting process based on time registration

Abnormalities in the collected data can result from the failure of blast furnace detection instruments and the abnormal operation of the blast furnace [19]. This study completes the abnormal data processing information collected during the blast furnace smelting process using the following three steps:

Step 1: Abnormal value detection. The 3σ criterion is adopted as the criterion to detect abnormal values in the blast furnace sample set, $X = \{x_2, \dots, x_n\}$. When the absolute difference between the detected and average value is greater than 3σ , it is marked as an abnormal value; σ can be expressed as follows:

$$\sigma = \sqrt{\sum_{i=1}^n e_i^2 / (n - 1)} = \sqrt{\sum_{i=1}^n (x_i - \bar{x})^2 / (n - 1)} \quad (4)$$

where n is a positive integer greater than or equal to 2; x_i is the i th measurement of index X ; \bar{x} is the average of all measurements of index X ; and e_i is the difference between the x_i and the \bar{x} .

Step 2: Outlier classification. This study compares the curves of the permeability index, cold air pressure, and silicon content of molten iron as indexes closely related to the molten iron content. Figure 3 shows that the molten iron silicon contents obtained from the eighteenth and thirty-second heats are at the lowest point, belonging to a suspicious point of abnormal value. Analyzing the changes

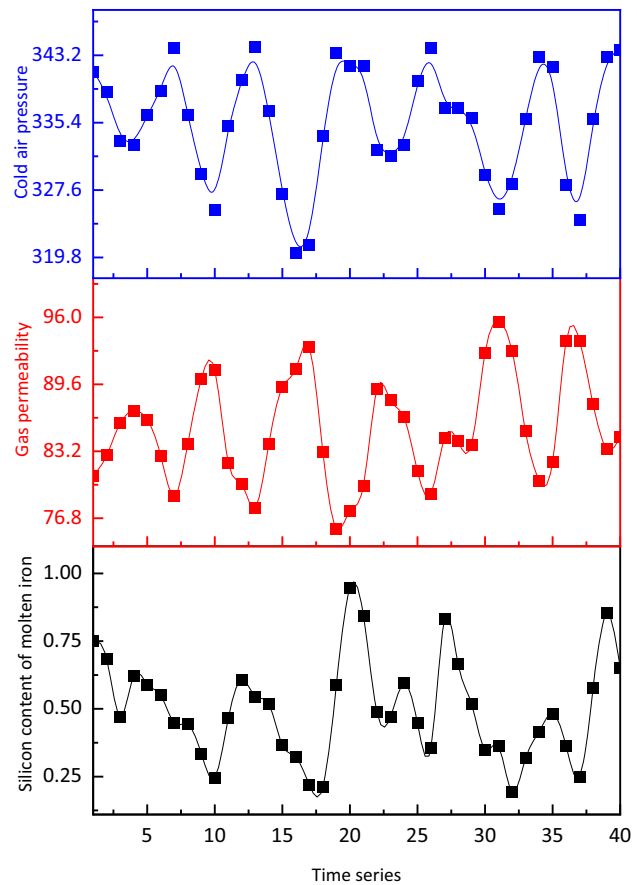


Fig. 3 Outlier determination

in the cold air pressure and permeability index—the cold air pressure decreases considerably, accompanied by an increase in the permeability index—shows signs of cooling furnace temperature. Consequently, it was determined that the suspicious points of these two abnormal data are non-abnormal values and vice versa.

Step 3: Normalization of indicator data. Based on Steps 1 and 2, the abnormal data caused by sensor failure are deleted, and the abnormal data caused by the abnormal operational state of the blast furnace are retained. The sample indexes after abnormal data processing differ owing to the differences in their dimensions. For example, the blast furnace permeability index range is [50, 100], while the cold air flow parameter range is [1800, 2300]. It is unreasonable to use them directly in predicting molten iron silicon content, as they can falsely influence the prediction results. Data normalization in Eq. (5) can be used to control the range of control parameters, such as the coal injection volume and air pressure, between [0,1] to improve the accuracy of subsequent model predictions.

$$x_i^* = \frac{x_i - \min(X)}{\max(X) - \min(X)} \quad (5)$$

where x_i^* is the standard value of x_i .

The data-driven technology and intelligent algorithms deeply mine the big data derived from the blast furnace smelting process to realize the accurate and continuous prediction of molten iron silicon content. The premise involves selecting the appropriate variables and their most appropriate time value. The correlation between the control variables, state variables, and molten iron silicon content under different time delay is obtained using the Spearman correlation analysis to realize the time registration between the index data. The principle of maximum correlation between the characterization parameters and molten iron silicon content under different time delay helps select the most appropriate time value of the variable.

Table 2 shows the sample indicator variable symbols and descriptions.

Step 1. Obtain 68 groups of index data—with a sampling period of 1 h—which correspond with their collection time and can be used to generate the initial sample set.

Step 2. Derive each index corresponding to the molten iron silicon content sequence under 0 delays based on eight different delay sequences. A sequence correspondence under four delays is shown in Fig. 4. The abscissa “0” refers to the current time, “1” refers to the time in the next 1 h, that is, the time of the nearest sampling in the future, and “− 1” refers to the time of the nearest sampling from the current time in history.

Step 3. Calculate and record the absolute correlation coefficient between each index in Fig. 4 and the molten iron silicon content sequence under eight different delays.

Step 4. Compare the absolute value of the correlation coefficient of each row in Table 3 and underline and mark bold to the largest value. If there is little difference between the two or three adjacent correlation coefficients and they are considerably higher than the coefficients under other delays, underline and mark bold to those coefficients too.

Step 5. Record the delay corresponding to the marked correlation coefficient in Table 3 and assign the delay directly to τ_i . Take the corresponding index data sequence as the sample input.

We collected a big data sample set from the smelting process of a blast furnace (3200 m³) in a steel plant in northern China. The samples comprised 55,000 hot metal sampling and testing results from November 1, 2019 to October 31, 2021 and the corresponding raw material and process information. Based on a sampling period of 1 h, a sample set using the variables shown in Table 2 as the input and the molten iron silicon content as the output for a given time sequence was constructed. Spearman analysis was used to calculate the correlation coefficient between the 68-index data shown in Table 2 (set time delay 0, 1, 2, 3, 4, 5, 6, and 7 h). After the above five steps, Table 3 is

Table 2 Sample indicator variable symbols and descriptions

No.	Variable name	Variable unit	Symbol
1	Raw material 1. Dafeng low strength coke	kg	$y_1(t - \tau_1)$
2	Raw material 2. Dafeng dry quenching coke	kg	$y_2(t - \tau_2)$
3	Raw material 3. Shanxi coke	kg	$y_3(t - \tau_3)$
4	Raw material 4. Japanese coke	kg	$y_4(t - \tau_4)$
5	Raw material 5. Yaxin coke	kg	$y_5(t - \tau_5)$
6	Raw material 6. Stem Yang coke	kg	$y_6(t - \tau_6)$
7	Raw material 7. Sinter	kg	$y_7(t - \tau_7)$
8	Raw material 8. Kaixin pellet	kg	$y_8(t - \tau_8)$
9	Raw material 9. Xinjing pellet	kg	$y_9(t - \tau_9)$
10	Raw material 10. Northeast pellet	kg	$y_{10}(t - \tau_{10})$
11	Raw material 11. Brazilian pellet	kg	$y_{11}(t - \tau_{11})$
12	Raw material 12. SP10 block ore	kg	$y_{12}(t - \tau_{12})$
13	Raw material 13. FMG block ore	kg	$y_{13}(t - \tau_{13})$
14	Raw material 14. Newman block ore	kg	$y_{14}(t - \tau_{14})$
15	Raw material 15. Limestone	kg	$y_{15}(t - \tau_{15})$
16	Actual cumulative batches		$y_{16}(t - \tau_{16})$
17	Expected batches	Circle	$y_{17}(t - \tau_{17})$
18	Joule ratio	%	$y_{18}(t - \tau_{18})$
19	Oxygen enrichment rate	%	$y_{19}(t - \tau_{19})$
20	Wind temperature	°C	$y_{20}(t - \tau_{20})$
21	Hot air pressure	kPa	$y_{21}(t - \tau_{21})$
22	Set coal injection rate	t/h	$y_{22}(t - \tau_{22})$
23	Actual coal injection rate	t/h	$y_{23}(t - \tau_{23})$
24	Cold air flow	m ³ /min	$y_{24}(t - \tau_{24})$
25	Blowing humidity	%	$y_{25}(t - \tau_{25})$
26	Oxygen enrichment	m ³ /h	$y_{26}(t - \tau_{26})$
27	Total oxygen flowrate	m ³ /h	$y_{27}(t - \tau_{27})$
28	Blast momentum	J/s	$y_{28}(t - \tau_{28})$
29	Total load [ore/coke (excluding coke)]	%	$y_{29}(t - \tau_{29})$
30	Fe/C	%	$y_{30}(t - \tau_{30})$
31	Cooling water temperature	°C	$y_{31}(t - \tau_{31})$
32	Cooling water flow	m ³ /h	$y_{32}(t - \tau_{32})$
33	Water temperature difference	°C	$y_{33}(t - \tau_{33})$
34	Coal injection rate	m/s	$y_{34}(t - \tau_{34})$
35	Feed rate	m/s	$y_{35}(t - \tau_{35})$
36	Calculated top gas volume	m ³ /h	$y_{36}(t - \tau_{36})$
37	Top temperature	°C	$y_{37}(t - \tau_{37})$
38	Top temperature range	°C	$y_{38}(t - \tau_{38})$
39	Top pressure	kPa	$y_{39}(t - \tau_{39})$
40	Differential pressure	kPa	$y_{40}(t - \tau_{40})$
41	Permeability index		$y_{41}(t - \tau_{41})$
42	Furnace body static pressure	kPa	$y_{42}(t - \tau_{42})$
43	Blanking point		$y_{43}(t - \tau_{43})$
44	Single layer coke thickness	m	$y_{44}(t - \tau_{44})$
45	Single layer mineral material thickness	m	$y_{45}(t - \tau_{45})$

Table 2 (continued)

No.	Variable name	Variable unit	Symbol
46	Theoretical combustion temperature	°C	$y_{46}(t - \tau_{46})$
47	Gas volume in tuyere area	m ³ /h	$y_{47}(t - \tau_{47})$
48	Bosh gas index	m ³ /min	$y_{48}(t - \tau_{48})$
49	Total heat supply	GJ	$y_{49}(t - \tau_{49})$
50	Heat supplied to lower part of cohesive zone	GJ	$y_{50}(t - \tau_{50})$
51	Proportion of heat at lower part of cohesive zone	%	$y_{51}(t - \tau_{51})$
52	Gasification coke quantity	t	$y_{52}(t - \tau_{52})$
53	Carbon monoxide concentration in tuyere area	%	$y_{53}(t - \tau_{53})$
54	Hydrogen concentration in tuyere area	%	$y_{54}(t - \tau_{54})$
55	Nitrogen concentration in tuyere area	%	$y_{55}(t - \tau_{55})$
56	Nitrogen oxide discharge of hot blast stove	m ³ /h	$y_{56}(t - \tau_{56})$
57	Average temperature of Section 6 water cooling	°C	$y_{57}(t - \tau_{57})$
58	Average temperature of Section 7 water cooling	°C	$y_{58}(t - \tau_{58})$
59	Average temperature of Section 8 water cooling	°C	$y_{59}(t - \tau_{59})$
60	Average temperature of Section 9 water cooling	°C	$y_{60}(t - \tau_{60})$
61	Average temperature of Section 10 water cooling	°C	$y_{61}(t - \tau_{61})$
62	Average temperature of Section 11 water cooling	°C	$y_{62}(t - \tau_{62})$
63	Average temperature of Section 12 water cooling	°C	$y_{63}(t - \tau_{63})$
64	Silicon content value of molten iron in last five times	%	$Y_{[Si]}(t - 5)$
65	Silicon content value of molten iron in last four times	%	$Y_{[Si]}(t - 4)$
66	Silicon content value of molten iron in last three times	%	$Y_{[Si]}(t - 3)$
67	Silicon content value of molten iron in last two times	%	$Y_{[Si]}(t - 2)$
68	Silicon content value of molten iron in last time	%	$Y_{[Si]}(t - 1)$

obtained, the order of delay being from small to large. We discern the following special cases.

- (1) The indexes with an absolute value of correlation coefficient greater than 0.8 with data series of the molten iron silicon content include the actual coal injection amount $\{y_{23}(t), y_{23}(t - 1)\}$ under 0 and 1 delay, the permeability index $\{y_{41}(t - 1)\}$ under 1 delay, the heat supplied to the lower part of the cohesive zone under 1 and 2 delay $\{y_{50}(t - 1),$

- $y_{50}(t - 2)\}$, the proportion of the heat supplied to the lower part of the cohesive zone under 1 delay in the total heat supply $\{y_{51}(t - 1)\}$, and the historical hot metal silicon content $\{Y_{[Si]}(t - 1)\}$ under 1 delay.
- (2) At 0 and 1 time delay, the correlation coefficient with the data series of the molten iron silicon content is relatively large for the air temperature $\{y_{20}(t), y_{20}(t - 1)\}$, actual coal injection $\{y_{23}(t), y_{23}(t - 1)\}$, oxygen enrichment $\{y_{26}(t), y_{26}(t - 1)\}$, total load $\{y_{29}(t), y_{29}(t - 1)\}$, permeability index $\{y_{41}(t), y_{41}(t - 1)\}$, and single layer coke thickness $\{y_{44}(t), y_{44}(t - 1)\}$.
- (3) At 1 and 2 time delay, the correlation with the data series of the molten iron silicon content is a relatively large indicator of the heat supplied to the lower part of the cohesive zone $\{y_{50}(t - 1), y_{50}(t - 2)\}$.
- (4) At 2 and 3 time delay, correlations are exhibited by the differential pressure $\{y_{40}(t - 2), y_{40}(t - 3)\}$ and the gas quantity at the air outlet $\{y_{47}(t - 2), y_{47}(t - 3)\}$.
- (5) At 1, 2, and 3 time delay, the correlations with the data series of the molten iron silicon content are relatively large indicators of the molten iron silicon content at historical moments $\{Y_{[Si]}(t - 1), Y_{[Si]}(t - 2), Y_{[Si]}(t - 3), Y_{[Si]}(t - 4), Y_{[Si]}(t - 5)\}$.
- (6) At 3 and 4 time delay, the correlation is relatively large for the total heat supply $\{y_{49}(t - 3), y_{49}(t - 4)\}$.
- (7) At 3, 4, and 5 time delay, the correlation is relatively large for the gas index of the furnace belly $\{y_{47}(t - 3), y_{47}(t - 4), y_{47}(t - 5)\}$.

4 Development of a dynamic and continuous prediction model for molten iron silicon content

Based on modern cybernetics, the blast furnace smelting process can be simplified into a multiple-input single-output system, and the molten iron silicon content can be predicted using the operating parameters. When the system is in a relatively stable state, the molten iron silicon content at $t + 1$ can be expressed as follows:

$$y(t) = \phi_1 y(t - 1) + \dots + \phi_n y(t - n_\phi) + \gamma_1 u(t - 1) + \dots + \gamma_n u(t - n_\gamma) + \theta_1 e(t - 1) + \dots + \theta_n e(t - n_\theta - 1) + \theta(t) \tag{6}$$

where $y(t)$ and $y(t - 1)$ denote the molten iron silicon content at t and $t - 1$, respectively; u denotes the input variable, that is, the operating parameter to be considered,

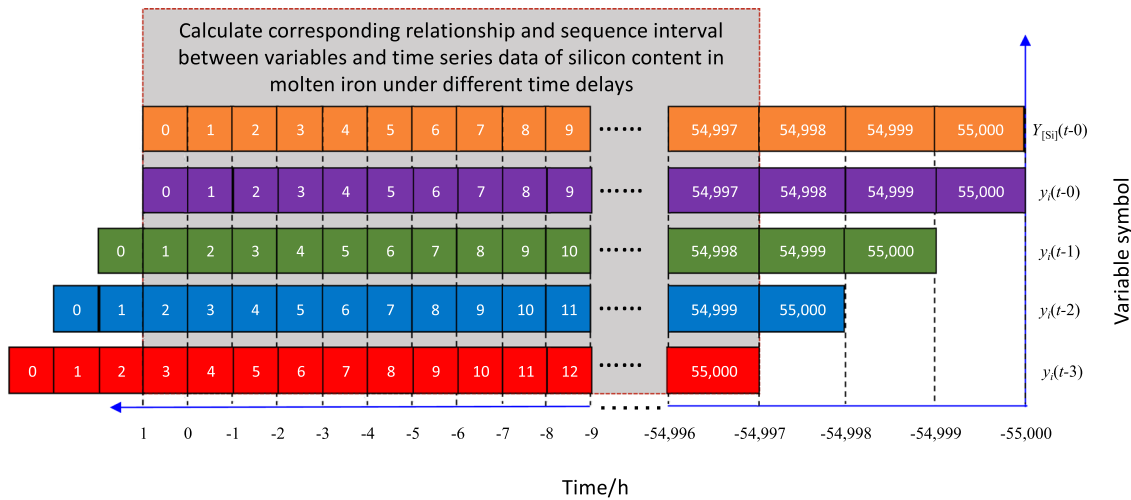


Fig. 4 Corresponding relationship diagram of correlation coefficients between index sequences under different delays to be solved

such as wind temperature and load; e denotes the error of the estimated value; φ , γ , and θ denote the model parameters; and φ_n , γ_n , and θ_n denote the response order of y , u and e , respectively.

Using Eq. (6), the dynamic data system model of hot metal silicon content can be obtained as shown by $\hat{y}(t)$ in Eq. (7) that represents the estimated value of $y(t)$.

$$\hat{y}(t) = \phi_1 y(t-1) + \dots + \phi_n y(t-n_\phi) + \gamma_1 u(t-1) + \dots + \gamma_n u(t-n_\gamma) + \theta_1 e(t-1) + \dots + \theta_n e(t-n_\theta-1) \tag{7}$$

In a complex blast furnace smelting process, the adjustment of one control variable can often cause changes in multiple state variables. In addition, each state variable can be affected by multiple control variables. Moreover, the static prediction model of molten iron silicon content based on historical data can be affected by the actual working conditions, resulting in poor robustness. By analyzing the time registration between big data in the blast furnace smelting process and studying the impact of different index data on state variables, the multi-path coupling relationship between variables, and the influence of each index on molten iron silicon content, the dynamic and continuous prediction of molten iron silicon content can be realized [20–22]. Through path optimization, the impact of the characterization parameters on different control variables as the starting point and the hot metal silicon content as the endpoint can be obtained. After retrieving the state variables in each path, we can use the characterization parameters before the state variables on each path as the input and the corresponding state variables as the output to predict each state variable. Finally, we integrate all control and state variables as the input samples to realize the

dynamic prediction of molten iron silicon content. This study designed an improved path optimization algorithm by coupling simulated annealing algorithm (SA) and genetic algorithm (GA). The implementation framework of the wavelet neural network algorithm can be used to construct a cascade dynamic and continuous prediction model of molten iron silicon content.

More indexes related to the molten iron silicon content should be considered to form index redundancy and improve the model prediction accuracy [23]. However, as more than one index data is possible in a physical sense, and sequences with different delays strongly correlate with the molten iron silicon content, it is necessary to re-plan the variables, dividing the index data into more than one index based on the delay. The sample input set for predicting the molten iron silicon content under the time sequence constructed in this study has 83 elements (Table 3), of which 40 are control variables, and 43 are state variables, including the molten iron silicon content at time delay 1, 2, and 3). Assuming that the set of control and state variables are B and C , respectively, then $A = B \cup C$. The elements in the sets of B and C can be expressed as follows:

$$B = \left\{ \begin{array}{cccc} y_1(t-7) & y_2(t-7) & y_3(t-7) & y_4(t-7) \\ y_5(t-7) & y_6(t-7) & y_7(t-7) & y_8(t-7) \\ y_9(t-7) & y_{10}(t-7) & y_{11}(t-7) & y_{12}(t-7) \\ y_{13}(t-7) & y_{14}(t-7) & y_{15}(t-7) & y_{16}(t-7) \\ y_{17}(t-5) & y_{18}(t-5) & y_{19}(t-6) & y_{20}(t-7) \\ y_{24}(t) & y_{25}(t) & y_{25}(t-1) & y_{26}(t) \\ y_{27}(t-6) & y_{28}(t) & y_{28}(t-1) & y_{29}(t-3) \\ y_{30}(t) & y_{31}(t) & y_{31}(t-1) & y_{32}(t) \\ y_{33}(t) & y_{34}(t) & y_{34}(t-1) & y_{35}(t-2) \\ y_{36}(t-3) & y_{37}(t-2) & y_{38}(t) & y_{39}(t-4) \end{array} \right\} \tag{8}$$

Table 3 Raw material control variable information for time registration

Variable symbol	Correlation coefficient between corresponding variables under different time delay and real-time silicon content in molten iron								Delay
	$\tau_i = 0$ h	$\tau_i = 1$ h	$\tau_i = 2$ h	$\tau_i = 3$ h	$\tau_i = 4$ h	$\tau_i = 5$ h	$\tau_i = 6$ h	$\tau_i = 7$ h	
$y_{19}(t - \tau_{19})$	0.2863	0.0466	0.0567	0.1066	0.0733	0.0316	0.0506	0.0720	0
$y_{21}(t - \tau_{21})$	0.1704	0.0909	0.0819	0.0334	0.0760	0.1106	0.0046	0.0518	0
$y_{25}(t - \tau_{25})$	0.1291	0.0423	0.0176	0.0426	0.0015	0.0517	0.0154	0.0767	0
$y_{27}(t - \tau_{27})$	0.2422	0.0921	0.0268	0.0835	0.0684	0.0573	0.0285	0.0170	0
$y_{28}(t - \tau_{28})$	0.7085	0.1106	0.3016	0.3772	0.3048	0.0983	0.0651	0.0028	0
$y_{33}(t - \tau_{33})$	0.2569	0.1373	0.0735	0.0576	0.0308	0.0668	0.1069	0.0873	0
$y_{42}(t - \tau_{42})$	0.2571	0.0302	0.0261	0.0128	0.0409	0.0426	0.0420	0.0997	0
$y_{46}(t - \tau_{46})$	0.6864	0.1709	0.1532	0.4369	0.2657	0.1682	0.4787	0.0902	0
$y_{53}(t - \tau_{53})$	0.5720	0.0665	0.0777	0.0559	0.0857	0.0923	0.0583	0.1214	0
$y_{54}(t - \tau_{54})$	0.5689	0.0008	0.1238	0.0717	0.0510	0.0504	0.0595	0.0538	0
$y_{55}(t - \tau_{55})$	0.5929	0.1686	0.0553	0.0675	0.0325	0.0400	0.1876	0.0748	0
$y_{20}(t - \tau_{20})$	0.7556	0.7572	0.1620	0.1976	0.2544	0.0639	0.0210	0.0332	0, 1
$y_{23}(t - \tau_{23})$	0.8963	0.8735	0.1601	0.2055	0.1501	0.0686	0.0865	0.0226	0, 1
$y_{26}(t - \tau_{26})$	0.7769	0.7397	0.0533	0.0727	0.0409	0.0339	0.0590	0.0090	0, 1
$y_{29}(t - \tau_{29})$	0.6640	0.6943	0.0884	0.0994	0.0218	0.0593	0.0830	0.0778	0, 1
$y_{41}(t - \tau_{41})$	0.7344	0.8752	0.2291	0.2893	0.1644	0.3565	0.5942	0.1801	0, 1
$y_{44}(t - \tau_{44})$	0.6635	0.6984	0.3835	0.3525	0.2837	0.0584	0.1662	0.0657	0, 1
$y_{36}(t - \tau_{36})$	0.0195	0.1812	0.0743	0.0880	0.0533	0.0986	0.0728	0.0881	1
$y_{37}(t - \tau_{37})$	0.0319	0.1779	0.0901	0.0942	0.0357	0.0192	0.0466	0.0527	1
$y_{38}(t - \tau_{38})$	0.0954	0.1811	0.0919	0.0803	0.0781	0.0786	0.0502	0.0149	1
$y_{39}(t - \tau_{39})$	0.0633	0.1243	0.0459	0.0713	0.0771	0.0819	0.0207	0.0590	1
$y_{43}(t - \tau_{43})$	0.2274	0.6347	0.2053	0.2053	0.2869	0.0802	0.0922	0.0584	1
$y_{51}(t - \tau_{51})$	0.1740	0.8189	0.4172	0.0625	0.2790	0.3606	0.0958	0.0920	1
$y_{50}(t - \tau_{50})$	0.0997	0.8570	0.8368	0.0925	0.0894	0.3634	0.0884	0.0608	1, 2
$y_{16}(t - \tau_{16})$	0.0374	0.0851	0.1423	0.0830	0.0958	0.0742	0.0735	0.0653	2
$y_{18}(t - \tau_{18})$	0.0630	0.2927	0.4433	0.1811	0.0557	0.0739	0.0403	0.0419	2
$y_{30}(t - \tau_{30})$	0.2934	0.1881	0.5845	0.2188	0.0993	0.0134	0.0790	0.0655	2
$y_{32}(t - \tau_{32})$	0.0927	0.0783	0.2035	0.0966	0.0667	0.0908	0.0408	0.0911	2
$y_{35}(t - \tau_{35})$	0.4058	0.3723	0.6049	0.3251	0.0854	0.2675	0.0996	0.3054	2
$y_{40}(t - \tau_{40})$	0.0603	0.0773	0.4947	0.4126	0.0586	0.0957	0.1707	0.0512	2, 3
$y_{47}(t - \tau_{47})$	0.0420	0.0868	0.3578	0.3718	0.2541	0.0824	0.0709	0.0948	2, 3
$y_{24}(t - \tau_{24})$	0.0049	0.0615	0.0211	0.1263	0.0558	0.0550	0.0255	0.0774	3
$y_{31}(t - \tau_{31})$	0.0896	0.0610	0.0620	0.3151	0.1291	0.0655	0.0835	0.0314	3
$Y_{57}(t - \tau_{57})$	0.0449	0.0664	0.0944	0.3152	0.0825	0.0801	0.0751	0.0251	3
$y_{58}(t - \tau_{58})$	0.0682	0.0764	0.0453	0.3480	0.0593	0.1308	0.1320	0.0732	3
$y_{59}(t - \tau_{59})$	0.0796	0.0570	0.0828	0.3196	0.0558	0.0853	0.0791	0.0771	3
$y_{60}(t - \tau_{60})$	0.0316	0.0385	0.0653	0.4892	0.0309	0.0563	0.0299	0.0752	3
$y_{61}(t - \tau_{61})$	0.0397	0.0897	0.0361	0.3478	0.0700	0.0935	0.0645	0.0776	3
$y_{62}(t - \tau_{62})$	0.0292	0.0817	0.0375	0.4580	0.0667	0.0752	0.0680	0.0509	3
$y_{63}(t - \tau_{63})$	0.1548	0.0317	0.0215	0.5183	0.0225	0.1369	0.0514	0.0658	3
$y_{49}(t - \tau_{49})$	0.1914	0.3408	0.3321	0.7228	0.7046	0.3165	0.0902	0.0749	3, 4
$y_{48}(t - \tau_{48})$	0.0390	0.1910	0.0972	0.4572	0.4769	0.4166	0.1576	0.0628	3, 4, 5
$y_{34}(t - \tau_{34})$	0.0684	0.1242	0.3933	0.2823	0.6852	0.4812	0.4591	0.1271	4
$y_{17}(t - \tau_{17})$	0.0283	0.0411	0.0327	0.1989	0.1784	0.3126	0.1481	0.1722	5
$y_{18}(t - \tau_{18})$	0.0487	0.0880	0.0535	0.0411	0.0473	0.3897	0.0103	0.1848	5
$y_{56}(t - \tau_{56})$	0.1194	0.3564	0.3552	0.3660	0.1399	0.5783	0.0247	0.1407	5

Table 3 (continued)

Variable symbol	Correlation coefficient between corresponding variables under different time delay and real-time silicon content in molten iron								Delay
	$\tau_i = 0$ h	$\tau_i = 1$ h	$\tau_i = 2$ h	$\tau_i = 3$ h	$\tau_i = 4$ h	$\tau_i = 5$ h	$\tau_i = 6$ h	$\tau_i = 7$ h	
$y_{19}(t - \tau_{19})$	0.0493	0.0614	0.0417	0.0276	0.0680	0.0280	0.1218	0.0307	6
$y_{17}(t - \tau_{17})$	0.0399	0.0211	0.0238	0.0342	0.0769	0.0687	0.3338	0.0335	6
$y_{22}(t - \tau_{22})$	0.0213	0.0521	0.1233	0.0096	0.1378	0.0562	0.2216	0.0361	6
$y_{45}(t - \tau_{45})$	0.0868	0.1142	0.1832	0.1613	0.0977	0.0760	0.4897	0.0886	6
$y_1(t - \tau_1)$	0.0776	0.0698	0.0196	0.0419	0.0128	0.0612	0.0478	0.1873	7
$y_2(t - \tau_2)$	0.0994	0.0826	0.0423	0.0406	0.0589	0.0469	0.0588	0.1945	7
$y_3(t - \tau_3)$	0.0859	0.0226	0.0319	0.0377	0.0714	0.0844	0.0620	0.2448	7
$y_4(t - \tau_4)$	0.0446	0.0688	0.0373	0.0888	0.0522	0.0576	0.0972	0.3988	7
$y_5(t - \tau_5)$	0.0309	0.0091	0.0228	0.0384	0.0702	0.0266	0.0436	0.1048	7
$y_6(t - \tau_6)$	0.0738	0.0543	0.0584	0.0657	0.0114	0.0003	0.0091	0.1270	7
$y_7(t - \tau_7)$	0.0414	0.0185	0.0611	0.0515	0.0220	0.0723	0.0470	0.1091	7
$y_8(t - \tau_8)$	0.0242	0.0300	0.0425	0.0068	0.0143	0.0757	0.0590	0.1518	7
$y_9(t - \tau_9)$	0.0343	0.0438	0.0619	0.0787	0.0216	0.0273	0.0561	0.1091	7
$y_{10}(t - \tau_{10})$	0.0529	0.0208	0.0769	0.0390	0.0194	0.0727	0.0754	0.1069	7
$y_{11}(t - \tau_{11})$	0.0777	0.0776	0.0846	0.0802	0.0863	0.0507	0.0781	0.1056	7
$y_{12}(t - \tau_{12})$	0.0279	0.0710	0.0622	0.0543	0.0010	0.0348	0.0665	0.1255	7
$y_{13}(t - \tau_{13})$	0.0479	0.0829	0.0259	0.0477	0.1041	0.0193	0.0440	0.1768	7
$y_{14}(t - \tau_{14})$	0.0341	0.0142	0.0846	0.0559	0.0440	0.0839	0.0106	0.1904	7
$y_{15}(t - \tau_{15})$	0.0774	0.0445	0.0130	0.0598	0.0439	0.0224	0.0555	0.1848	7
$y_{16}(t - \tau_{16})$	0.0888	0.0672	0.0498	0.0765	0.0788	0.0948	0.0531	0.1695	7
$y_{20}(t - \tau_{20})$	0.0474	0.0361	0.0336	0.0474	0.0434	0.0530	0.0176	0.1067	7
$y_{52}(t - \tau_{57})$	0.1565	0.1133	0.0459	0.0819	0.1870	0.0772	0.0892	0.5908	7
$Y_{[Si]}(t - \tau_{69})$	1.0000	0.8024	0.7360	0.5953	0.2541	0.0920	0.2176	0.1481	1, 2, 3

$$C = \left\{ \begin{array}{cccc} y_{21}(t-2) & y_{22}(t-6) & y_{23}(t-2) & y_{40}(t-2) \\ y_{41}(t-1) & y_{42}(t-1) & y_{43}(t-1) & y_{44}(t-1) \\ y_{45}(t-2) & y_{45}(t-3) & y_{46}(t) & y_{46}(t-1) \\ y_{47}(t) & y_{48}(t-1) & y_{49}(t) & y_{49}(t-1) \\ y_{50}(t-6) & y_{51}(t) & y_{52}(t-2) & y_{52}(t-3) \\ y_{53}(t-3) & y_{53}(t-4) & y_{53}(t-5) & y_{54}(t-3) \\ y_{54}(t-4) & y_{55}(t-1) & y_{55}(t-2) & y_{56}(t-1) \\ y_{57}(t-7) & y_{58}(t) & y_{59}(t) & y_{60}(t) \\ y_{61}(t-5) & y_{62}(t-3) & y_{63}(t-3) & y_{64}(t-3) \\ y_{65}(t-3) & y_{66}(t-3) & y_{67}(t-3) & y_{68}(t-3) \end{array} \right\} \quad (9)$$

Based on the sets shown in Eqs. (8) and (9), a weighted directed graph of the silicon content in the iron can be constructed, with the weights and directions of the directed graph being specified as follows.

(1) Taking all elements in the set as nodes and the correlation coefficient between elements as the weight, the correlation coefficient matrix between the data series of each variable is 83×83 (since the number of variables studied is 83). However, the

calculation method is simple and can be solved quickly using SPSS software; hence, it is not shown in this paper.

(2) The effect of the silicon content on each direction of molten iron can be determined. From any element, the arrow always points to an element with less delay. If the delays of two elements are equal, the two elements are the starting and endpoint of each other.

(3) Starting from any element, the path that can reach the molten iron silicon content at the current time through the directed graph can be considered as one path. The travel route can only move forward without turning back. This path reflects the information transfer direction and influence relationship among the characteristic parameters of blast furnace.

(4) The indexes to determine the advantages and disadvantages of a path are the least cost (eliminating the correlation between variables) and longest path (providing more sample input redundancy), that is,

the sum of path weights is the smallest on the premise of traversing as many nodes as possible.

GA and SA are intelligent algorithms used to solve complex programming problems. A GA and SA coupled blast furnace characterization parameter path optimization algorithm was designed to solve the multi-path coupling problem between variables. The proposed algorithm adopts the strong overall searchability of GA and the strong local searchability of SA to circumvent the disadvantages of insufficient stability of GA and the time-consuming overhead of SA. Based on the correlation between each index under different time delay sequences and the correlation with the molten iron silicon content under different time sequences, a weighted directed graph of the characterization parameters of the molten iron silicon content can be constructed. Several best influence paths in-line with the actual production situation of the blast furnace can be excavated using different control variables as the starting point, laying the foundation for the follow-up intelligent learning of the wavelet neural network algorithm.

The path optimization algorithm of the GA and SA coupling technique is described as follows.

- (1) Using any control variable as the starting point and the molten iron silicon content at time t as the endpoint, the initial population can be randomly generated.
- (2) Determine the fitness functions. Set the fitness function as shown in Eq. (10), where α_i denotes the correlation between the i th and $(i + 1)$ th parameter, k is a coefficient, and m denotes the number of individuals in the population.
- (3) The roulette method can be adopted. Based on individual fitness, some individuals with greater fitness are selected from the population with the probability of p'_i to form a mating pool, as expressed in Eq. (11), where N is the population, and F_i is the fitness of the i th individual.
- (4) The adaptive probability function can cross, mutate, and update the mating pool. The adaptive probability function can be expressed as shown in Eq. (12), where f denotes the larger fitness of the two individuals crossing, f_{avg} denotes the average fitness value, f_{max} denotes the best fitness, and p_1 and p_2 are constants.
- (5) SA can be applied to the new individuals generated after crossover and mutation. The accepted individuals and their parents conduct elite selection to form their offspring population.
- (6) Repeat execution of Steps 2–5. Stop when the fitness function value no longer increases.

$$F = \sum_{i=1}^{m-1} \frac{k\alpha_i}{m-1} \quad (10)$$

$$p'_A = \frac{k/F_i}{\sum_{i=1}^N k/F_i} \quad (11)$$

$$p_1 = \begin{cases} (f_{\text{max}} - f)/(f_{\text{max}} - f_{\text{avg}}), & f > f_{\text{avg}} \\ p_2, & f \leq f_{\text{avg}} \end{cases} \quad (12)$$

This study used the wavelet neural network algorithm to learn the sample set and mine the quantitative relationship between sample inputs and outputs. Though the wavelet and back propagation (BP) neural network algorithms are multilayer feedforward networks, the kernel functions are wavelet and sigmoid functions, respectively. Wavelet analysis can better determine the local characteristics of the signal by transforming the wavelet basis function. The corresponding weight and activation threshold from the input to the hidden layer can be replaced by the scale expansion and time translation factors of the wavelet function. Moreover, the gradient correction method can modify the weight and wavelet basis function parameters of the network, giving the wavelet neural network stronger nonlinear approximation abilities.

The training steps of the wavelet neural network algorithm are as follows:

- (1) Randomly initialize the scaling factor, translation factor, and network connection weight of the wavelet function, and set the network learning rate.
- (2) Divide the samples into training and test samples. The training samples are used for network training, and the test samples to test the network prediction accuracy.
- (3) Input the training samples into the network, to calculate the prediction output and the error between the network and expected output.
- (4) The network weight and wavelet function parameters can then be corrected based on the error, making the network predicted value close to the expected value in the future.
- (5) Determine whether the algorithm ends. If not, return to 3.

Thus, starting from each control variable, that is, the elements in set \mathbf{B} , the optimal path to reach the molten iron silicon content can be found using the improved GA and SA. The corresponding nodes of elements in set \mathbf{C} can be retrieved by integrating the optimal path results. The characterization parameters before the node are used as the prediction input of the state variables [24]. The prediction value of elements in \mathbf{C} can be obtained using the wavelet neural network and is substituted into the prediction input

data of the molten iron silicon content to realize dynamic prediction [25]. The dynamic and continuous prediction model of molten iron silicon content based on path optimization is shown in Fig. 5.

The dynamic and continuous prediction model of molten iron silicon content has the following advantages:

- (1) *Supplement the data set under low delay.* During the early stage of blast furnace operation, the state variables with a small time delay with the molten iron silicon content have not yet been obtained. Therefore, the corresponding state variables are predicted through the known control variables that supplement the input data of the prediction model to realize a dynamic prediction model.
- (2) *Dynamic precise control.* Based on the operational mechanism of the blast furnace and actual operation of workers, this model aims to realize the dynamic control and early prevention of furnace temperature. The workers can predict changes in corresponding state parameters by assuming the input control parameters to predict changes in the furnace temperature. Thus, the goal of a stable and abundant furnace temperature and conditions can be achieved.

5 Results and discussion

5.1 Optimal path for silicon content prediction in hot metal

The primary goal of the research is to find the optimal prediction path for the molten iron silicon content. To verify the excellent properties of the improved objective algorithm (GA and SA) in path finding, we performed simultaneous search operations using the three algorithms and compared their performance in terms of iteration times and fitness functions. The smaller the number of iterations and the larger the fitness function, the better the performance. This metric is equivalent to the metric for determining the merit of a path.

By analyzing the elements in set **B**, a longer path can be considered using the elements in the subset **B'** as the starting point, as follows:

$$\mathbf{B}' = \left\{ \begin{array}{cccc}
 y_1(t-7) & y_2(t-7) & y_3(t-7) & y_4(t-7) \\
 y_5(t-7) & y_6(t-7) & y_7(t-7) & y_8(t-7) \\
 y_9(t-7) & y_{10}(t-7) & y_{11}(t-7) & y_{12}(t-7) \\
 y_{13}(t-7) & y_{14}(t-7) & y_{15}(t-7) & y_{16}(t-7) \\
 y_{20}(t-7) & y_{19}(t-6) & y_{27}(t-6) & \end{array} \right\} \tag{13}$$

In Table 4, the above 19 elements were used as the path starting points, and the three algorithms were applied

simultaneously to set **A**. The number of iterations and the value of the fitness functions for each optimal path were obtained for comparative analysis. Based on the data summarized in Table 4, the following results were obtained:

- (1) *Comparative analysis of the number of iterations.* The GA achieved a stable value of fitness function at an average of 68 iterations in determining the optimal path, while the SA algorithm required 126 iterations. Based on the relationship between the number of iterations and the running time of the algorithm, the SA algorithm took twice as long to run as GA. The average number of iterations of the GA and SA algorithm was close to that of GA, suggesting that the target algorithm inherited the advantage of the rapid convergence of GA.
- (2) *Comparative analysis of fitness values.* The average fitness function value of the GA for searching the optimal path for the 19 different starting points in Table 4 was 0.24004, while that of the SA algorithm was 0.28407, with an improvement of 18.34%. The average fitness function value for the target algorithm was 0.30021, which is significantly better than those of the individual GA and SA algorithms. Thus, the target algorithm inherited the global rapid search capability of GA and the local optimal value-seeking capability of SA.
- (3) *Overall.* The GA and SA algorithm exhibits excellent path finding performance and quality, achieving a comparable number of iterations to the GA algorithm and optimal fitness values. Paths (1) $y_4(t-7) \rightarrow Y_{[Si]}(t)$, (2) $y_7(t-7) \rightarrow Y_{[Si]}(t)$, (3) $y_8(t-7) \rightarrow Y_{[Si]}(t)$, (4) $y_{19}(t-6) \rightarrow Y_{[Si]}(t)$, and (5) $y_{22}(t-6) \rightarrow Y_{[Si]}(t)$ have higher values of fitness function. Overall, the fitness value achieved using the GA and SA for path (2) was considerably better than that of the two comparison algorithms and had the highest fitness values of all paths.

The molten iron silicon content prediction path aims to eliminate the correlation between variables and reduce the number of input indicators while considering the coupling synergy of multiple variables in terms of duration and structure. Thus, a cascade of continuous molten iron silicon content predictions is achieved with coupled state variable node studies to determine that this model works best.

The state variable permeability index ($y_{41}(t)$) and theoretical combustion temperature ($y_{46}(t)$) with “0” delay as the molten iron silicon content at the current moment were selected as evaluation indicators to verify this assumption. We compared the forecast accuracy of $y_{41}(t)$ and $y_{46}(t)$ on paths (1)–(5) and selected the path with the highest forecast accuracy for both state variables as the optimal path.

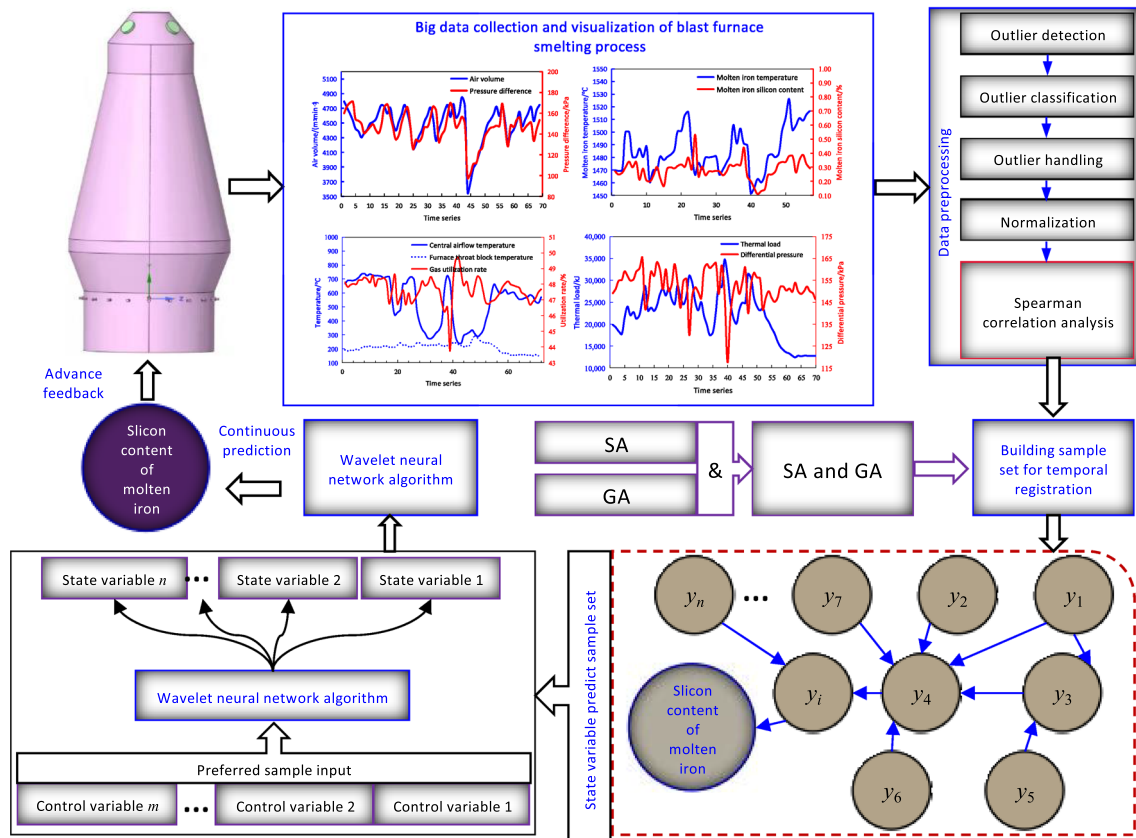


Fig. 5 Dynamic prediction model of molten iron silicon content based on path optimization

We used the wavelet neural network algorithm to learn the sample data on paths (1)–(5) to obtain comparison plots of the forecast results of the permeability index and theoretical combustion temperature. The actual values and error plots when forecasting the permeability index under the five paths are shown in Figs. 6 and 7, and those for the theoretical combustion temperature are shown in Figs. 8 and 9. The wavelet neural network structure used in this study was 5 – 30 – X. The five nodes in the input layer indicate the number of steps in the prediction sequence. The 30 and X nodes in the hidden and output layers indicate the number of state variables on the prediction path.

Figure 6 represents the comparison of the prediction effects of the permeability state variables achieved under the five preferred paths. Since the starting point of path (2) is the raw material information and the lag time is the longest (7 h), the path can traverse more selective nodes from the starting point to the endpoint, so that the sample set is guaranteed to be rich in content while seeking the optimal selection. It is verified through simulation prediction tests that the sample set formed based on path (2) is the most superior and can make the prediction results closer to the actual values. In addition, Fig. 7 shows the distribution of the permeability prediction error under the five preferred paths, which shows that the prediction error of the

algorithm using the sample set formed by path (2) is within $[- 1, 1]$, the prediction error of path (3) is within $[- 5, 5]$, and the prediction error of the remaining three preferred paths is within $[- 20, 20]$. Figures 8 and 9, which use the theoretical combustion temperature as the prediction node in the data representation, again confirm that the best prediction is achieved using path (2) to form the sample set.

Figures 6, 7, 8 and 9 show that the predicted and actual values are the closest to path (2), $y_7(t - 7) \rightarrow Y_{[Si]}(t)$, for the permeability index and theoretical combustion temperature forecasts. Consequently, path (2) was used as the optimal path for the molten iron silicon content prediction.

5.2 Predicting molten iron silicon content

The sample set for prediction can be divided into three categories as follows:

- (1) *Class 1* data use all the variables in Table 2 as a sample set, including instant and historical data collected during the blast furnace smelting process. To realize the advanced prediction of the molten iron silicon content, we pay more attention to the effective predictions of $Y_{[Si]}(t + 1)$, $Y_{[Si]}(t + 2)$,

Table 4 Comparison of three paths optimization algorithms

Path start	Path end	GA		SA		GA and SA		Optimal algorithm	
		Iteration	Fitness	Iteration	Fitness	Iteration	Fitness	Iteration	Fitness
$y_1(t - 7)$	$Y_{[Si]}(t)$	67	0.14212	108	0.20088	68	0.21700	GA	GA and SA
$y_2(t - 7)$	$Y_{[Si]}(t)$	69	0.22943	101	0.29006	73	0.28406	GA	SA
$y_3(t - 7)$	$Y_{[Si]}(t)$	57	0.11774	174	0.20449	58	0.28863	GA	GA and SA
$y_4(t - 7)$	$Y_{[Si]}(t)$	55	0.30194	168	0.32084	64	0.34884	GA	GA and SA
$y_5(t - 7)$	$Y_{[Si]}(t)$	64	0.24146	132	0.28387	74	0.25927	GA	SA
$y_6(t - 7)$	$Y_{[Si]}(t)$	77	0.20486	76	0.27900	80	0.29407	GA	GA and SA
$y_7(t - 7)$	$Y_{[Si]}(t)$	73	0.38799	199	0.40224	95	0.45861	GA	GA and SA
$y_8(t - 7)$	$Y_{[Si]}(t)$	64	0.28184	136	0.34580	65	0.34013	GA	SA
$y_9(t - 7)$	$Y_{[Si]}(t)$	73	0.10342	110	0.16085	65	0.13620	GA and SA	SA
$y_{10}(t - 7)$	$Y_{[Si]}(t)$	72	0.21807	118	0.21828	77	0.24038	GA	GA and SA
$y_{11}(t - 7)$	$Y_{[Si]}(t)$	74	0.21130	180	0.29228	68	0.31398	GA and SA	GA and SA
$y_{12}(t - 7)$	$Y_{[Si]}(t)$	78	0.29678	119	0.31826	59	0.34549	GA and SA	GA and SA
$y_{13}(t - 7)$	$Y_{[Si]}(t)$	78	0.17567	100	0.23590	72	0.29940	GA and SA	GA and SA
$y_{14}(t - 7)$	$Y_{[Si]}(t)$	61	0.20465	94	0.28792	60	0.27606	GA and SA	SA
$y_{15}(t - 7)$	$Y_{[Si]}(t)$	66	0.29645	144	0.33889	70	0.34945	GA	GA and SA
$y_{16}(t - 7)$	$Y_{[Si]}(t)$	60	0.20028	185	0.25666	78	0.21207	GA	SA
$y_{20}(t - 7)$	$Y_{[Si]}(t)$	62	0.17866	135	0.20910	77	0.21050	GA	GA and SA
$y_{19}(t - 6)$	$Y_{[Si]}(t)$	67	0.38919	118	0.40428	61	0.40992	GA and SA	GA and SA
$y_{22}(t - 6)$	$Y_{[Si]}(t)$	72	0.37880	116	0.34765	74	0.34990	GA	GA and SA
Average		68	0.24004	126	0.28407	69	0.30021	GA	GA and SA

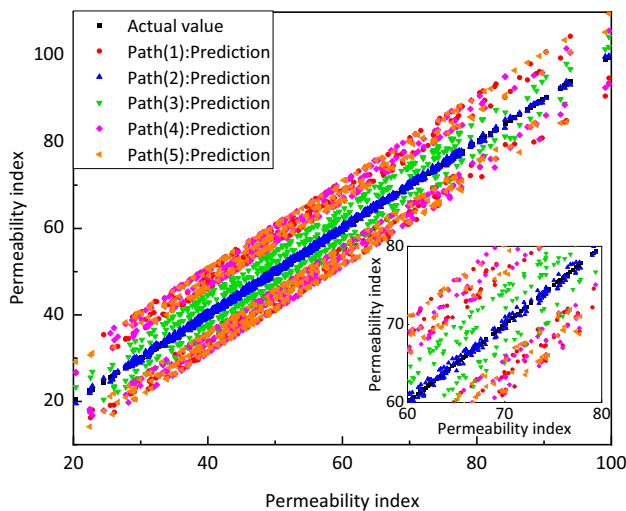


Fig. 6 Comparison of prediction results of ventilating index under 5 paths

$Y_{[Si]}(t + 3)$, $Y_{[Si]}(t + 4)$, and $Y_{[Si]}(t + 5)$. The input of the sample output time ahead or the synchronous sample input index when predicting $Y_{[Si]}(t + 1)$ can be the data from the actual historical data aligned to moment $t + 1$ when the sample input indicators in Table 2 are control variables. For example, the

kinetic energy of the blast (y_{28}) control variable can be used directly as a sample input with its corresponding time series $y_{28}(t + 1)$. When the sample input indicator is a state variable, the sample input indicators in Table 2 at time t can only be selected. For example, the theoretical combustion temperature (y_{46}) state variable can only be used as a sample input at time t with $y_{46}(t)$, not with its temporal counterpart $y_{46}(t + 1)$.

- (2) *Class 2* data are immediate and historical data based on the control variables selected after optimal filtering and the state variables that pass through the path. The selection constraints for the indicators are the same as those of *Class 1* data. Certain state variables cannot be applied directly, and the number of variables is only reduced by path finding.
- (3) *Class 3* data are immediate and historical data for control variables selected based on optimal path filtering and predicted values for state variables. The selection of indicators for *Class 3* data would not have the constraints of *Class 1* and *Class 2* data. The state variables corresponding to the time series $Y_{[Si]}(t + 1)$, $Y_{[Si]}(t + 2)$, $Y_{[Si]}(t + 3)$, and $Y_{[Si]}(t + 4)$ are obtained via prediction, then used as inputs, so that the prediction process could achieve dynamic

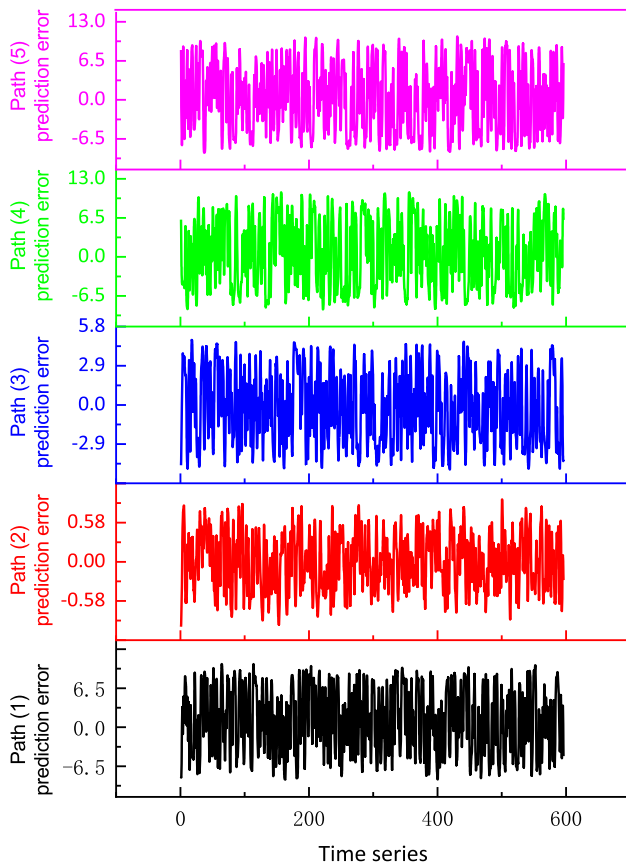


Fig. 7 Comparison of prediction error of permeability index under 5 paths time series

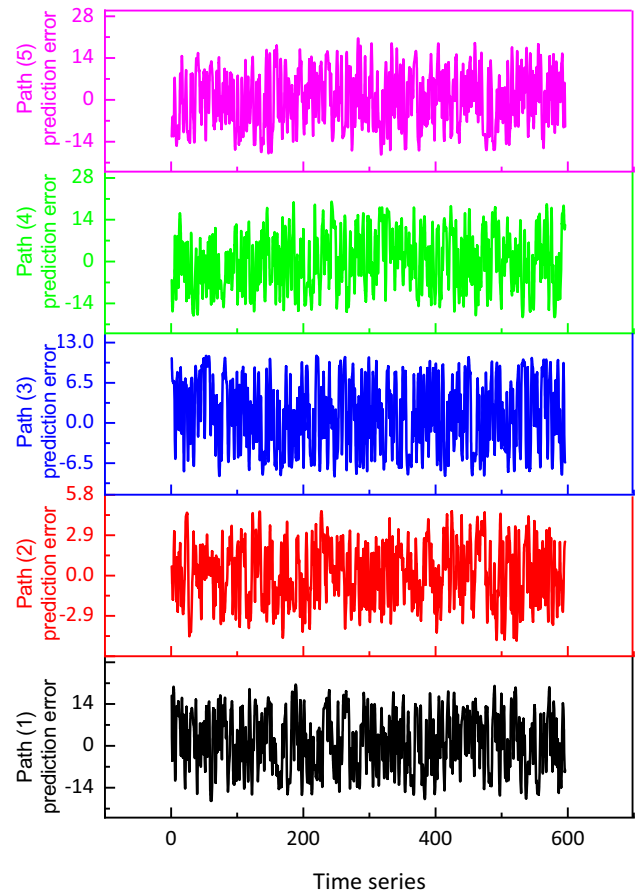


Fig. 9 Comparison of theoretical combustion temperature of prediction error of permeability index under 5 paths time series

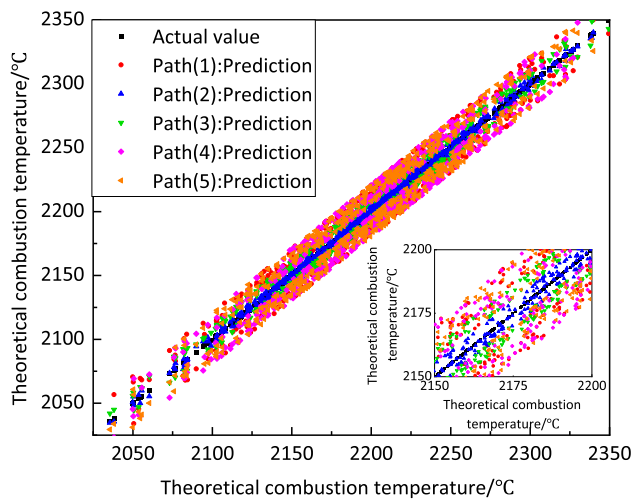


Fig. 8 Comparison of theoretical combustion temperature prediction results under 5 paths

self-renewal of the sample set. The wavelet neural network algorithm intelligently learns the above three classes of sample sets to construct multi-step prediction models for the molten iron silicon content $Y_{[Si]}(t)$, $Y_{[Si]}(t + 1)$, $Y_{[Si]}(t + 2)$, $Y_{[Si]}(t + 3)$,

$Y_{[Si]}(t + 4)$, and $Y_{[Si]}(t + 5)$. A comparison of the prognosis results and analysis is shown in Figs. 10–15.

When comparing the real-time forecast results, since Class 2 and 3 sample sets are similar at this stage, the forecast accuracy is also equivalent. The forecast using Class 1 is the worst. Firstly, it considers too many redundant variables, resulting in a small proportion of effective information. Secondly, the learning is poor because the parameter selection of the wavelet neural network algorithm depends on the few useful sample data for path optimization.

When comparing the 1- to 5-step ahead prediction results, the prediction accuracy using the Class 3 sample set always shows a considerable advantage. The forecast accuracy of Class 1 and 2 sample sets is low, with a maximum error boundary. We conclude that some of the control variables in the historical data play a role in frame support, that is, the empirical control of operations such as adjusting the fabric and improving the blast can change the molten iron silicon content trends. However, accurate

research, consideration, and control cannot be achieved from an accuracy perspective.

The average error values were analyzed to determine the validity of the proposed method. Table 5 confirms the advantages and extension value of the proposed step-by-step silicon content prediction technique. The mean absolute error and coefficient of variation increase, and the prediction hit rate decreases on the sequence of real-time forecasts in molten iron silicon content to 5-step ahead forecasts in all three classes. The results reflect the dependence of forecast accuracy on the sample set validity, with a strong correlation between the big data collected during the blast furnace smelting process and the molten iron silicon content. Using Class 1 and 2 data, the average absolute error and hit rate in the predicted molten iron silicon content from 1- to 5-step ahead were in the range of [0.241, 0.254] and [17.5%, 23.0%], respectively. Although the hit rate of real-time prediction was above 94%, it was ineffective in providing a reference for the overcasting of the molten iron silicon content regulation. Class 3 data achieved over 87% of the 5-step ahead forecasts, with 91.16% of the forecasts hitting 1-step ahead. Class 3 data were a dynamic sample set that achieved good prediction accuracy; however, the accuracy gradually decreased with accumulating prediction errors in the state variables, with silicon content as the endpoint.

In summary, the wavelet neural network algorithm is an intelligent algorithm suitable for learning sample sets with temporal correlation. The prediction accuracy of the same intelligent algorithm varies considerably depending on the sample sets category. $y_7(t - 7) \rightarrow Y_{[Si]}(t)$ was used as the optimal path for the prediction of molten iron silicon content. The sample set was dynamically updated to achieve over 87% molten iron silicon content prediction accuracy 5-step ahead.

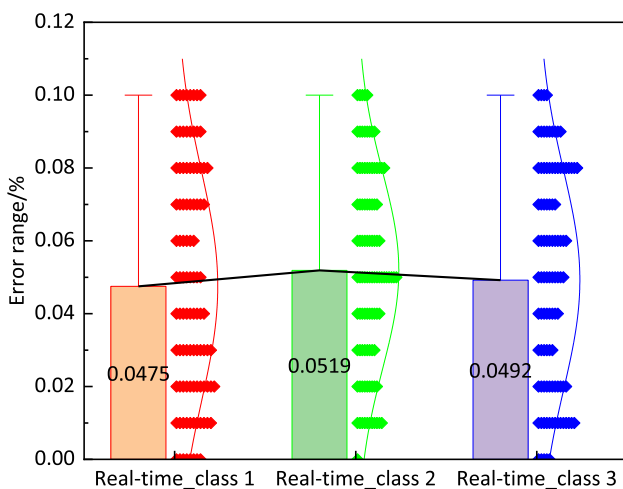


Fig. 10 Comparison of real-time prediction effect

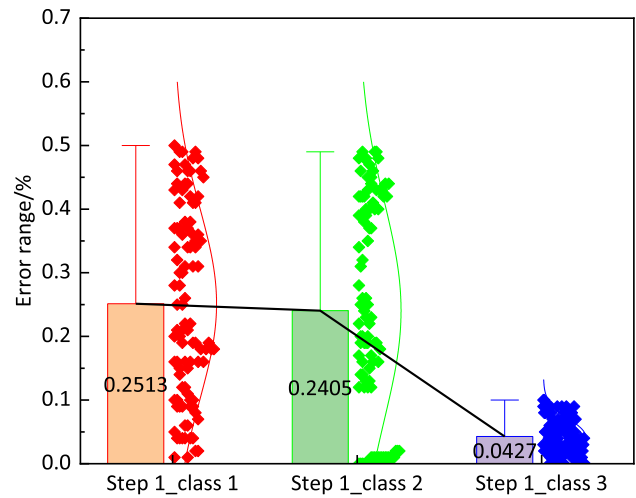


Fig. 11 Comparison of step 1 ahead prediction effect

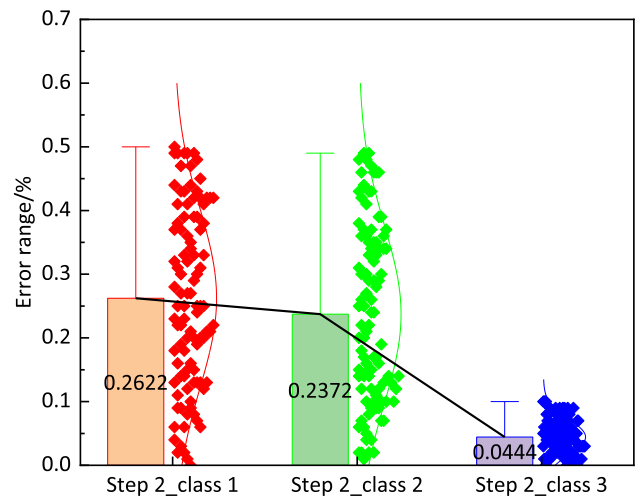


Fig. 12 Comparison of step 2 ahead prediction effect

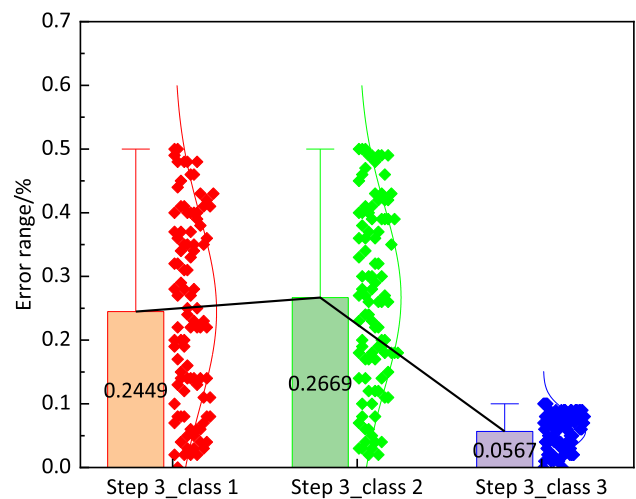


Fig. 13 Comparison of step 3 ahead prediction effect

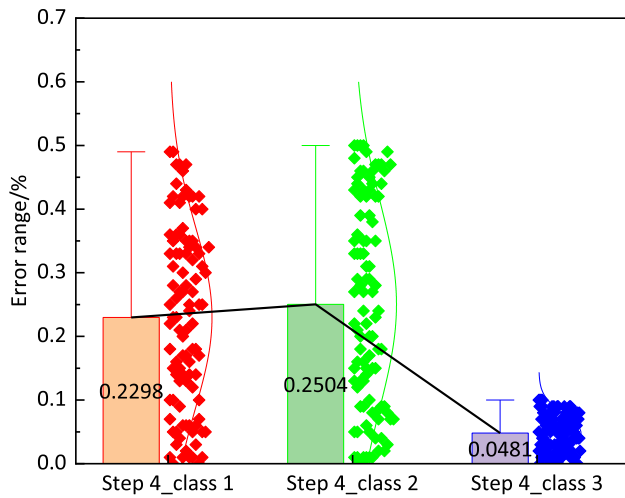


Fig. 14 Comparison of step 4 ahead prediction effect

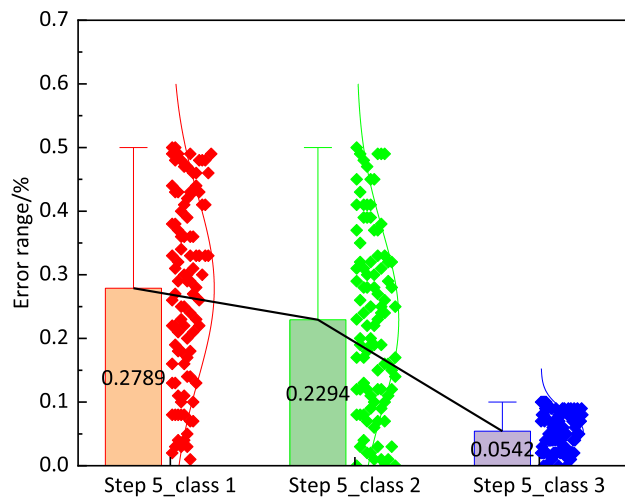


Fig. 15 Comparison of step 5 ahead prediction effect

6 Conclusions

1. The optimal selection of sample indicators, based on the principle of maximum correlation and time alignment, was a prerequisite for ahead-of-time, continuous, and accurate prediction of the molten iron silicon content. In addition, it contributed to creating a good data ecological environment for using intelligent algorithms.
2. Adopting the GA and SA coupling algorithm, we optimized the molten iron silicon content prediction path and reduced the sample input indicator, improving the effectiveness of the sample set information. Moreover, it lowered the complexity of the intelligent data learning algorithm, directly enhancing the learning efficiency of the wavelet neural network algorithm.
3. Based on the optimization of the molten iron silicon content forecasting path, a self-learning forecasting model based on control variables as sample inputs and lagging state variables in the path as sample outputs. The model is the driving force to drive the dynamic update of the sample set and the guarantee to achieve 1, 2, 3, 4 and 5-step ahead prediction of the silicon content of molten iron.
4. The proposed cascade model with coupled state variable nodes achieved a forecasting accuracy of 91.16% in 1-step ahead predictions and a hit rate of 87.41% in 5-step ahead predictions.
5. The model formed a paradigm comprising data information self-processing, prediction path self-optimizing, and state variable node information self-updating. Moreover, the step-by-step and continuous prediction of molten iron silicon content can help develop intelligent control systems for blast furnaces.

Table 5 Comparison of step-by-step prediction effect of molten iron silicon content in blast furnace based on learning sample differences

Categories	Class 1			Class 2			Class 3		
	MAE	CV	Hit rate/%	MAE	CV	Hit rate/%	MAE	CV	Hit rate/%
Real-time	0.0499	0.5671	94.56	0.0491	0.5741	95.41	0.0494	0.5692	95.24
1-step	0.2440	0.5766	21.94	0.2482	0.5759	22.96	0.0486	0.5708	91.16
2-step	0.2466	0.5857	20.58	0.2474	0.5789	21.94	0.0507	0.5792	89.63
3-step	0.2482	0.5863	20.07	0.2533	0.5895	20.41	0.0526	0.5889	89.63
4-step	0.2485	0.5908	19.56	0.2509	0.5995	19.90	0.0488	0.5948	88.10
5-step	0.2494	0.6028	17.52	0.2417	0.6062	19.90	0.0505	0.6007	87.41

MAE—Mean absolute error; CV—coefficient of variation

Acknowledgements This work was financially supported by the National Natural Science Foundation of China (Grant No. 52074126) and Tangshan Science and Technology Plan Project (Grant No. 22130201G).

Declarations

Conflict of interest This manuscript has not been published or presented elsewhere in part or in entirety and is not under consideration by another journal. We have read and understood your journal's policies, and we believe that neither the manuscript nor the study violates any of these. There are no conflicts of interest to declare.

References

- [1] J. Li, C. Hua, Y. Yang, X. Guan, *IEEE Trans. Syst. Man Cybern. Syst.* 52 (2022) 1087–1099.
- [2] Z.Q. Cui, Y. Han, A.M. Yang, Y.Z. Zhang, S. Zhang, *Metalurgical Industry Automation* 45 (2021) No. 3, 51–57.
- [3] Z.Q. Cui, Y. Han, C.M. Lu, Y.F. Wu, M.S. Chu, *Computational Intelligence and Neuroscience* 2021 (2021) 1767308.
- [4] Y. Han, J. Li, X.L. Yang, W.X. Liu, Y.Z. Zhang, *Complexity* 2018 (2018) 8079697.
- [5] Y. Han, W.G. Han, K. Zeng, *IEEE Trans. Ind. Inform.* 18 (2021) 3397–3405.
- [6] Y. Han, C.J. Zhang, L. Wang, Y.C. Zhang, *IEEE Trans. Ind. Inform.* 16 (2019) 2640–2650.
- [7] J. Li, W.Q. Liu, Y. Han, W.X. Liu, A.M. Yang, F. Li, D.L. Li, *IEEE Trans. Ind. Inform.* 17 (2020) 4107–4116.
- [8] N.A. Spirin, A.A. Polinov, I.A. Gurin, V.A. Beginyuk, S.N. Pishnograev, A.S. Istomin, *Metallurgist* 63 (2020) 898–905.
- [9] J. Li, C. Hua, Y. Yang, X. Guan, *IEEE Trans. Fuzzy Syst.* 29 (2021) 1654–1666.
- [10] P. Zhou, W. Li, H. Wang, M. Li, T. Chai, *IEEE Trans. Cybern.* 50 (2020) 4783–4795.
- [11] J. Li, C. Hua, Y. Yang, X. Guan, *IEEE Trans. Ind. Electron.* 65 (2018) 4933–4942.
- [12] J.H. Song, C.J. Yang, Z. Zhou, W.H. Liu, S.Y. Ma, *CIESC J.* 67 (2016) 729–735.
- [13] G.M. Cui, R. Chen, K. Yu, Y. Zhang, *Control Engineering of China* 27 (2020) 1901–1906.
- [14] C.H. Jiang, C. Xu, W.H. Gui, K. Jiang, *Acta Autom. Sin.* 48 (2022) 194–206.
- [15] C.J. Zhang, Y. Han, S.Y. He, A.M. Yang, J.C. Chang, *Chinese Journal of Scientific Instrument* 39 (2018) No. 1, 24–33.
- [16] X.G. Liu, S.H. Luo, Y.H. Liu, X.F. Wu, *Control Theory and Applications* 23 (2006) 391–396.
- [17] J. Zhang, K. Wang, Z. Wang, L. Yang, L.J. Meng, *J. Iron Steel Res.* 32 (2020) 720–726.
- [18] W.G. Kong, J.H. Liu., Z.J. He, *J. Iron Steel Res.* 33 (2021) 375–384.
- [19] Z. Dong, H. Jia, *Chinese Journal of Scientific Instrument* 41 (2020) No. 2, 126–134.
- [20] Z.Q. Xu, M.F. Ren, L. Cheng, R. Li, G.W. Yan, *Chinese Journal of Scientific Instrument.* 42 (2021) No. 11, 279–287.
- [21] E. Lughofer, R. Pollak, C. Feilmayr, M. Schatzl, S. Saminger-Platz, *Steel Res. Int.* 92 (2021) 2100078.
- [22] D. Fojtik, J. Tuma, P. Faruzel, *Ironmak. Steelmak.* 48 (2021) 1226–1238.
- [23] Z. Abdel Hamid, S. Abd El Rehim, M. Ibrahim, *Anti-Corrosion Methods and Materials* 64 (2017) 479–485.
- [24] J. Staudte, J.M. Maigne, F. Del Frate, D. Loison, S. Cremel, *Metall. Res. Technol.* 111 (2014) 17–23.
- [25] Y.I. Uchida, Y. Kishimoto, Y. Miki, T. Uchida, R. Tsutsumi, T. Ueno, *ISIJ Int.* 56 (2016) 986–994.

Springer Nature or its licensor (e.g. a society or other partner) holds exclusive rights to this article under a publishing agreement with the author(s) or other rightsholder(s); author self-archiving of the accepted manuscript version of this article is solely governed by the terms of such publishing agreement and applicable law.